Check for updates

Facile development of copper ferrite nanospheres for UV light-driven photocatalytic degradation of cloxacillin sodium

Muhammad Naeem, [ab] Faheem Haider,[a] Adnan Ashraf, *[a] Saeed Ahmed, *[c] Khalid Mujasam Batoo, [d] Waseeq Ahmad Siddiqui, [e] Muhammad Imran,[b] Muhammad Asam Raza, [f] Muhammad Pervaiz[g] and Sajjad Hussain[h]

Copper ferrite nanoparticles (CuFe$_2$O$_4$ NPs) have multiple applications in various fields. Herein, a co-precipitation method under mild basic conditions has been used to develop CuFe$_2$O$_4$ NPs. The obtained precipitates were annealed at 500 °C for 4 hours to form copper ferrite. The synthesis of CuFe$_2$O$_4$ NPs was initially confirmed by UV-visible spectroscopy. The presence of specific functional groups like Fe−O was found at 593 cm^{-1} using Fourier transform infrared spectroscopy. The tetrahedral crystal structure for the CuFe$_2$O$_4$ NPs has been confirmed by X-ray diffraction analysis. The nanosphere-like morphology was confirmed by field emission scanning electron microscopy and the average calculated size of the nanoparticles is ∼45 nm and the pH$_{PZC}$ for the CuFe$_2$O$_4$ NPs is 6.67. The synthesized CuFe$_2$O$_4$ NPs were used for UV light-mediated degradation of cloxacillin sodium (CLX). The degradation of CLX was optimized under different sets of conditions including times of exposure of the drug with the catalyst under UV light, pH values, concentrations, and dosages of the catalyst. The total organic carbon (TOC) confirms 39% degradation of the drug, which is converted into inorganic carbon (IC) and in line with other experimental results. This study provides new insight into the use of copper ferrite to overcome pharmaceutical pollution of water bodies.

Introduction

Water pollution has been a major global issue.[1] Different types of waste from various sources, including industrial, agricultural, medical, domestic, and home waste, can cause water pollution.[2] In many developing countries, there is no proper system to monitor the discharged water from industries to make it safe for the environment.[3] The contaminated water from industries drains into the open channels of canals, rivers, and oceans. The dissolving of waste materials in water bodies is very dangerous and toxic for human health.[4] Many pollutants,

including primary and secondary, can cause water pollution.[5] Industrial waste is now dumped into water faster because of urbanization. New hazards to the environment and human health are various kinds of effluents. The characteristics of organic contaminants, including high toxicity and lower solubility, are serious concerns to human health.[6] In particular, in many developing countries, wastes from the pharmaceutical industry have become an annoyance with adverse consequences for the environment and human health. In this regard, a major factor of water pollution is caused by pharmaceutical drugs. Inappropriate disposal of hospital and pharmaceutical industry waste seriously threatens communities.[7] Researchers have been paying considerable attention to the excessive use of drugs in recent years because of their hazardous impact. These have been regarded as the main organic contaminants frequently found in wastewater.[2]

It has been well established that antibiotic drugs have several hazardous effects on the environment that can affect both animals and humans.[8] Harmful effects of drugs in the environment are usually observed even at very low concentrations.[9] CLX is a member of the penicillin family of antibiotic drugs, extensively used to treat infections caused by bacteria in animals and humans.[10] Conventionally applied biological wastewater

[a] Department of Chemistry, The University of Lahore, Lahore, Pakistan.
E-mail: adnanashraf7772@gmail.com
[b] Centre for Inorganic Chemistry, School of Chemistry, University of the Punjab, Lahore, Pakistan
[c] Department of Chemistry, University of Chakwal, Chakwal-48800, Pakistan.
E-mail: saeedahmedlaghari@chemist.com
[d] College of Science, King Saud University, P.O. Box-2455, Riyadh-11451, Saudi Arabia
[e] Institute of Chemistry, University of Sargodha, Sargodha-40100, Pakistan
[f] Department of Chemistry, The University of Gujrat, Gujrat, Pakistan
[g] Department of Chemistry, Govt. College University, Lahore, Pakistan
[h] Graphene Research Institute and Institute of Nano and Advanced Materials Engineering, Sejong University, Seoul, 143-747, Republic of Korea

treatment procedures cannot remove CLX from water bodies. Previously, several conventional methods such as electro-dialysis,[11] filtration,[12] adsorption,[13] electrodeionization,[14] electro-chemical reduction,[15] and biological treatments have been used for the degradation of all these kinds of organic pollutants present in waste water, which are not appropriate to remove drug contents from wastewater.[16] Physical methods like filtration or sedimenta-tion are considered safe ways, but they produce sludge, which produces further secondary pollution.[17]

Furthermore, these methods are complicated and costly, and by transferring pollutants among fluids, various wastes and by-products are produced, making wastewater treatment difficult using conventional methods.[18] The most effective and efficient method is the advanced oxidation process with the aid of photocatalysts.[19,20] The use of photocatalysts under UV-visible light is very fruitful for the treatment of wastewater[21,22] with drug-based pollutants.[23]

One powerful approach for reducing pollutants in the environment is the development of nanoparticles as catalysts.[24–26] The basic properties like charge transport, band gap, quantum effect and surface states of the material change as its size decreases from bulk to nanoscale.[27] The photocatalysis techni-que has garnered significant attention in the environmental refining industry because of its unique characteristics, which include low cost, easy operating environment, and energy effi-ciency. When light irradiation activates the semiconductor behaviors of photocatalysts, the electrons and holes are pro-duced. Spinel ferrites are effective agents for the photocatalysis and photodegradation of dyes and drugs, because of their catalytic activity, lower solubility, stable crystalline structure, and exceptional magnetic activity. These characteristics can also make it simple to recover nanoparticles like $ZnFe_2O_4$,[28] $CoFe_2O_4$,[29] $MgFe_2O_4$,[30] $MnFe_2O_4$,[31] $CuFe_2O_4$ and nickel ferrite ($NiFe_2O_4$) from solutions using an external magnetic field.[32,33] Due to their ferrimagnetic activity, ferrites are primarily complex oxides containing ferric ions that are categorized as magnetic materials. The interactions between metallic ions at specific locations with oxygen ions in the oxide crystal structure give rise to the magnetic properties of the ferrites. Snoek and associates at the Philips Research Laboratories in the Nether-lands enhanced the range of ferrites between 1945 and 1993.[34]

Ferrites can immediately eliminate contaminants using easily available visible light, making them the most effective light-sensitive photocatalysts. One of the most important ways to reduce water contamination is to use photocatalysts for wastewater retreatment. It was previously found that $CuFe_2O_4$ NPs were a 75% efficient photocatalyst for rhodamine B dye.[35] Since the physical properties of $CuFe_2O_4$ nanoparticles such as phase transitions, electrical switching, semi-conductivity, mag-netic properties, and chemical stability can alter in response to varying environmental circumstances, they are the ideal spinel ferrite.[36] $CuFe_2O_4$ nanoparticles have been employed in the production of lithium-ion rechargeable batteries, magnetic resonance imaging materials, photocatalysts for hydrogen evo-lution using visible light, energy storage materials, coupling reaction catalysts, CO_2 reduction catalysts, photoanodes for solar water oxidation, supports for enzyme immobilization, and catalysts in nanomedicine for the treatment of breast cancer.[37]

Copper ferrite is widely used in numerous fields, such as photocatalysis, high-density magnetic storage media, high-performance electromagnetic devices, and heterogeneous catalysis. Its use has also expanded to include antibacterial properties, magnetic resonance imaging, magnetic separation of cancer cells, biomedicine, and medication delivery.[38] With a band gap of less than 2.5 eV, ferrites with remarkable magnetic properties have enhanced photocatalytic activities and absorb significant visible light.[39] The possible strategies for producing ferrite nanoparticles must have the maximum rate of recombi-nation properties as spinel ferrite nanoparticles like $CuFe_2O_4$ may degrade organic pollutants.[40] Several applications of cop-per ferrite as a photocatalyst have recently been studied, including H_2 production, and degradation of rhodamine B and methylene blue.[41] Furthermore, $CuFe_2O_4$ nanoparticles show potential applications for lithium batteries in high-freq-uency devices, magnetic memory, drug delivery, sensors, and anode materials.[42] $CuFe_2O_4$ is found in a tetragonal shape and has an inverse spinel structure. Each unit cell encloses eight Cu-II ions in octahedral sites and sixteen ferric (Fe-II and Fe-III) ions equally distributed among tetrahedral and octahedral sites.[43] The magnetic properties of the NPs adapt due to the Cu-II ions as the magnetic moments of Fe-II and Fe-III cancel each other.[44] This phenomenon of charge distribution plays an important role in their potential applications as sensors, for electrical applications, and as active photocatalysts.[45]

Sol–gel, co-precipitation, hydrothermal, and solid-state methods are commonly used to synthesize $CuFe_2O_4$ NPs.[46] However, these synthetic procedures have some limitations, such as toxicity, high bioaccumulation, and not being eco-friendly.[47] Compared to other conventional methods of synth-esis, chemical co-precipitation to synthesize nanoparticles of $CuFe_2O_4$ has more advantages due to its simplicity, productivity, high purity, stability, uniformity, low cost, and controllable particle size, shape, and composition.[48]

The $CuFe_2O_4$ NPs were successfully prepared using the co-precipitation method in this research work. The novelty of these prepared nanoparticles includes their good photocatalytic effi-ciency for the degradation of the least explored cloxacillin sodium (CLX) drug, easy preparation, good recyclability, high structural and thermal stability, and easy separation. The prepared $CuFe_2O_4$ nanoparticle photocatalyst was characterized for structural, ele-mental, and morphological properties. Furthermore, the photoca-talytic activity of the prepared sample was evaluated for the degradation of CLX, and various process parameters for the reac-tion were also optimized. Scheme 1 shows the formation of copper ferrite and its photocatalytic degradation of pharmaceuticals.

Results and discussion

Structure of copper ferrite

FT-IR spectroscopy of the synthesized nanoparticles after calci-nation was employed to investigate the various functional
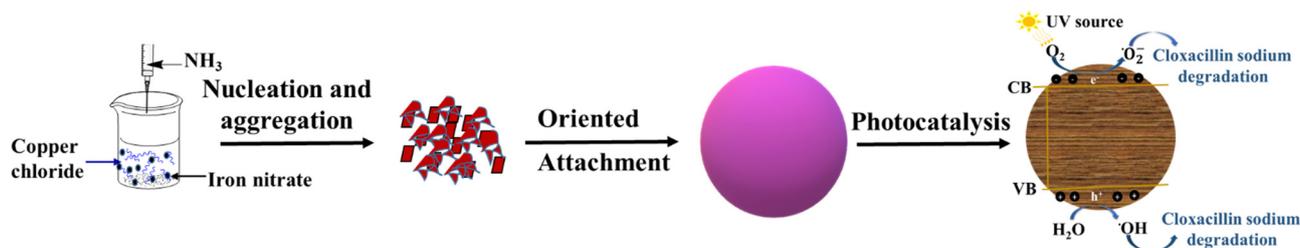
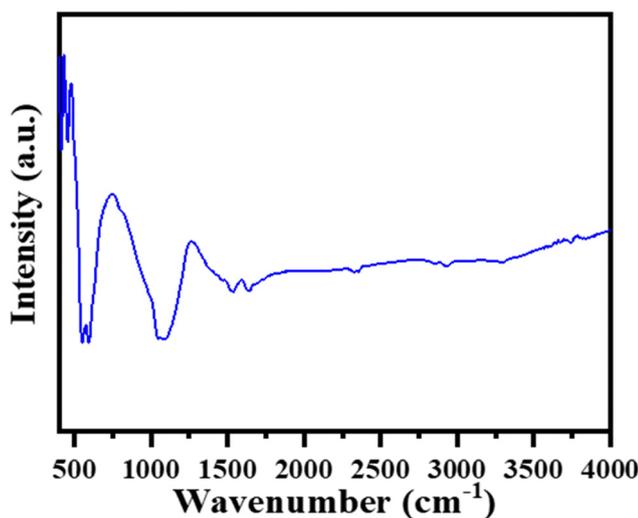**Scheme 1** Formation mechanism for copper ferrite and degradation of pharmaceuticals.

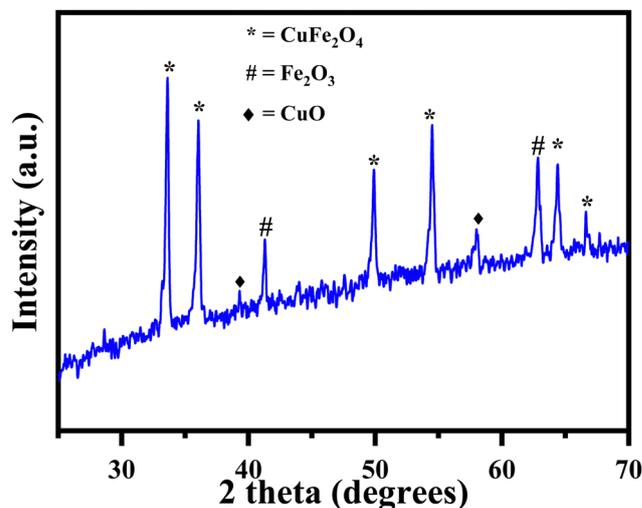**Fig. 1** FT-IR spectroscopy of the synthesized $CuFe_2O_4$ NPs after calcination.

Fig. 2 X-Ray diffraction pattern of the $CuFe_2O_4$ NPs after calcination.

groups. Fig. 1 displays the FT-IR spectrum of the $CuFe_2O_4$ NPs. The high-frequency band 593 cm^{-1} indicates the deformation of Fe–O in tetrahedral and octahedral sites. In comparison, the low-frequency band at ~ 456 cm^{-1} is ascribed to the deformation of Fe–O in the octahedral hematite site.[49] The OFe–OH bond was observed at 1091 cm^{-1}. The two bands at 1536 cm^{-1} and 1644 cm^{-1} correspond to metal hydroxyl group bending vibration.[50]

The XRD pattern of the $CuFe_2O_4$ NPs is shown in Fig. 2. As can be seen, the X-ray diffraction for the prepared sample has six major strong peaks at 2θ = 33.62°, 36.06°, 49.92°, 54.49°, 64.35°, and 66.63° (JCPDS card # 34-0425), which describe the tetragonal shape of copper ferrite.[51] Moreover, two peaks are seen at 2θ = 39.31° and 58.1° corresponding to the monoclinic CuO phase plane (JCPDS card # 80-1916).[52] The peaks of Fe_2O_3 were still found at 2θ = 41.34° and 62.77°, which corresponded to the well-accepted JCPDS card (33-0664).[53] Based on X-ray diffraction data, the Debye–Scherrer equation was used to calculate the crystallite size of copper ferrite based on eqn (1).

$$D = \frac{K\lambda}{\beta \cos \theta} \qquad (1)$$

where D, λ, β, k, and θ are assigned to the average crystallite size of NPs, the X-ray wavelength, the line broadening at the half

summit of the max of the XRD, shape factor, and the Bragg angle, respectively.

Morphology of copper ferrite

The surface morphology of the nanoparticles was investigated using SEM analysis. Fig. 3(A) and (B) show SEM images of the $CuFe_2O_4$ NPs. The magnetic properties of the $CuFe_2O_4$ NPs indicated aggregation.[54] The morphology of the NPs was recognized as spherical and cubic shapes because over half of the particles were prepared when the reaction was mixed under a magnetic field. In contrast, other NPs did not have the chance to grow up in a heating oven through a hydrothermal reaction. As shown in Fig. 3B, the $CuFe_2O_4$ NPs have an average diameter size of about 45 nm. Further, the elemental composition of the synthesized $CuFe_2O_4$ was confirmed by EDX analysis as shown in Fig. 4, which is well in agreement with the literature data.

PL spectroscopy

The separation–recombination process of the photoinduced electron–hole (e^-/h^+) pair was monitored by photoluminescence spectroscopy. The PL spectrum of the $CuFe_2O_4$ NPs presented in Fig. 5 has sharp bands, which are designated to Fe^{3+} charge transfer and O^{2-} ions surrounding the octahedral sites. The PL spectrum exhibits four PL transitions at 455, 539, 576, and 659 nm. The transitions at 455 nm might be assisted
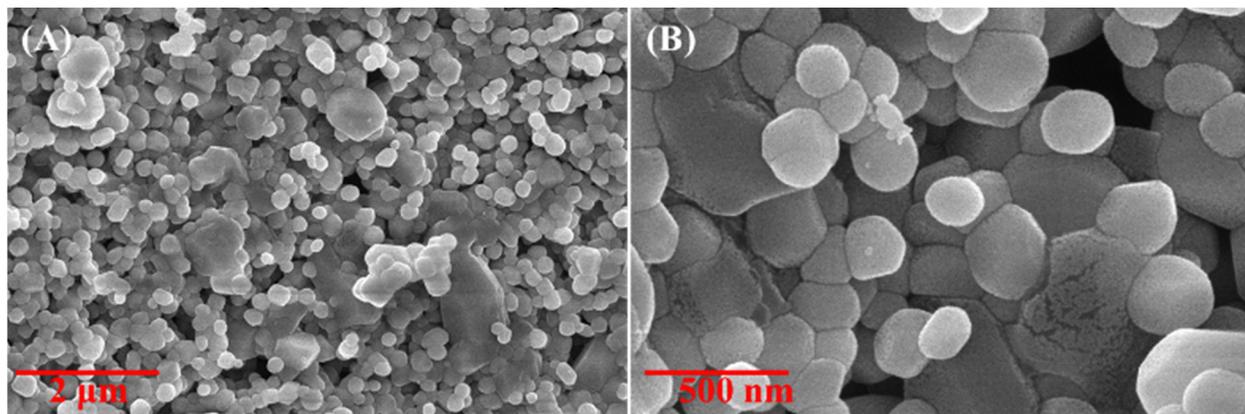
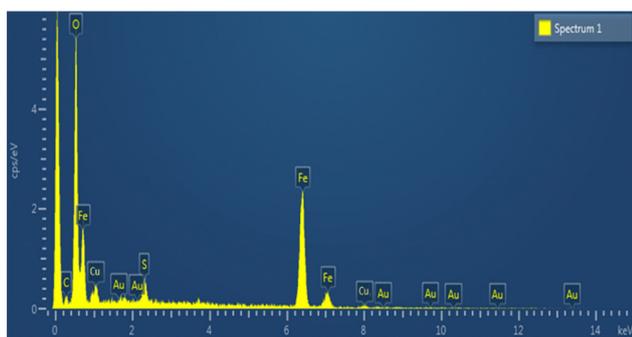**Fig. 3** Field emission scanning electron microscopy of the formed CuFe$_2$O$_4$ NPs after calcination.

Fig. 4 EDX spectrum for the CuFe$_2$O$_4$ NPs.

Fig. 5 Photoluminescence spectrum of CuFe$_2$O$_4$ NPs.

by the intra-band gap defects and oxygen vacancies. These defects are responsible for affording donor levels near the conduction band edge of the metal oxide. The peaks observed at 539 and 576 nm are relatively small intensity peaks that indicate the exciton separation efficiency and are designated to transition between the conduction band and defect sites on the surface of the catalyst. The peak found at 659 nm indicates the least charge carrier separation. The obtained results are in good agreement with the literature data.[55]

Surface area

The surface area analysis of the CuFe$_2$O$_4$ nanocomposite was conducted through a comprehensive examination using nitrogen adsorption and desorption analyses. The adsorption isotherm, presented in Fig. 6, is a key indicator of the material's porosity and structure. This isotherm's classification as type IV, according to the IUPAC criteria,[56] confirms that CuFe$_2$O$_4$ can be categorized as a mesoporous material. It can be seen that the CuFe$_2$O$_4$ nanomaterial synthesized *via* the co-precipitation method exhibits a large specific surface area of 65.24 m^2 g^{-1}.[57]

Determination of point of zero charge (pH$_{PZC}$)

The pH of the point of zero charge is a crucial factor that directly indicates the acidity and basicity of the adsorbent along with the net charge on the catalyst. The equal concentration of
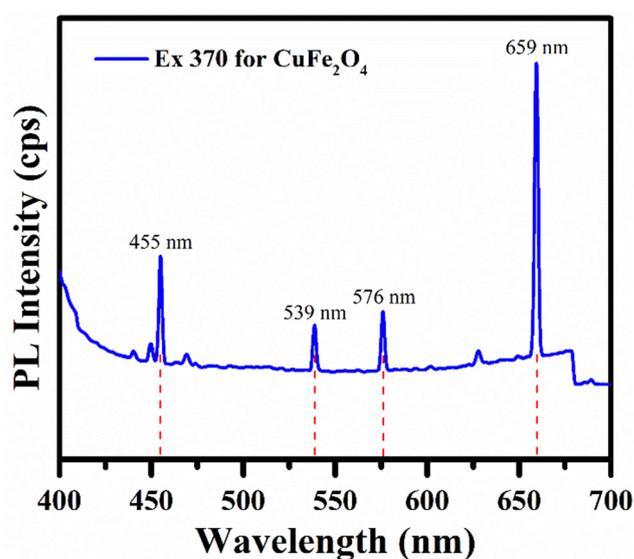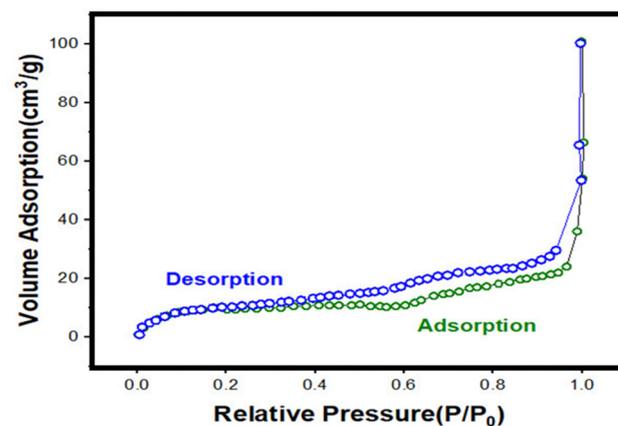

Fig. 6 Low-temperature nitrogen adsorption–desorption isotherms for CuFe$_2$O$_4$.
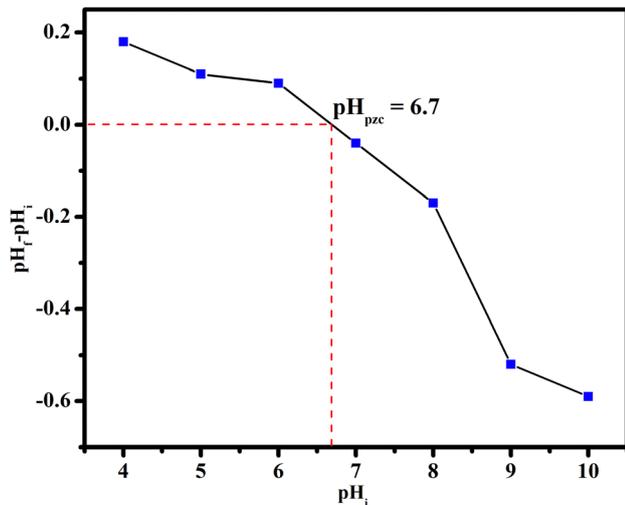
Fig. 7 Point of zero charge (PZC) of copper ferrite NPs.

Fig. 9 Effect of solution pH on the degradation efficiency.

positive and negative charges on the surface of the adsorbent can be determined by pH_{PZC}.[58] The experimental results are presented in Fig. 7, which indicates that the pH_{PZC} of copper ferrite is 6.67. The presence of positive charge on the surface of copper ferrite is expected below this pH, while negative charges may be available above this pH.

Photocatalytic degradation of CLX

Effect of irradiation time on degradation. Fig. 8 shows the photocatalytic behavior of copper ferrite towards CLX. There is an increase in the photocatalytic degradation efficiency with time in the first three min of irradiation time and then equilibrium is attained. The highest degradation efficiency of 40% was attained and remained constant for up to ten min.

Effect of pH. The influence of pH on antibacterial degradation can be stated by evaluating the properties of both the catalyst and the antibiotics at various pH levels.[59] The pH value of the solution influenced the binding sites on the adsorbent
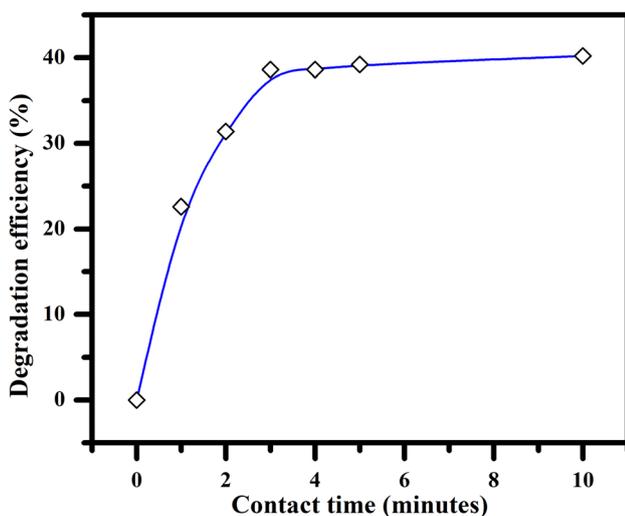
surface, and this adsorption process enhanced the chemical reaction between CLX molecules on the adsorbent particles *via* electrostatic interactions. The results are shown in Fig. 9, which shows that the maximum degradation occurs at pH 8. Furthermore, it is suggested by the results that the adsorption of CLX on the surface of the $CuFe_2O_4$ NPs is the key factor. The adsorption of CLX at pH 8 is higher, and therefore higher degradation was observed because of decomposition of the beta-lactam ring at this pH.[60] However, the lowest adsorption of the CLX on the surface of the catalyst at pH 9 could be due to saturation of negatively charged ions resulting in the decline of the degradation percentage.[60]

Effect of concentration of drug and dosage of catalyst. The dosage of the catalyst and the concentration of the drug may affect the degradation of CLX molecules. Fig. 10 shows the degradation efficiency of copper ferrite at different concentrations (1, 2, 3, 4, and 5 ppm) of the drug with different dose amounts of catalyst (0.05, 0.1, 0.15, and 0.2 mg mL^{-1}). The catalyst effectively degrades CLX up to the maximum value of
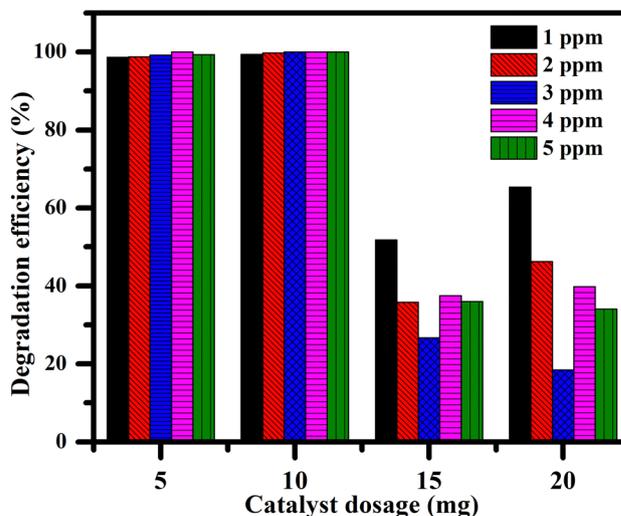

Fig. 8 Degradation efficiency with time at room temperature.

Fig. 10 Effect of catalyst dosage and CLX concentration on the degradation efficiency.

Table 1 Comparison of different synthesis methods and targeted pollutant degradations using copper ferrite

S. no.	Synthetic methods	Morphology	Targeted pollutant	Degradation efficiency (%)	Ref.
1	Hydrothermal	Cubic	Methylene blue	95.9	61,62
2	Co-precipitation	Irregular blocks	Lignin	92.21	63
3	Co-precipitation	Irregular blocks	Lignin	58.77	
4	Solid reaction process	Irregular blocks	Lignin	71.24	
5	Ethylene glycol-assisted sol–gel process	Irregular blocks	Lignin	49.73	
6	Hydrothermal process	Irregular blocks	Lignin	58.34	
7	Green genesis approach	Spherical shaped	Methylene blue dye	88	64
8	Co-precipitation	Sphere-shaped	2,4-Dichloro phenoxy acetic acid	88.9	65
9	Hydrothermal	Cubic	Methylene blue dye	95.9	66
10	*Via* a one-step hydrothermal	Spherical and cubic shapes	Nitroanilines	—	67
11	Sol–gel method	Spherical	Atenolol	90	68
12	Sol–gel	Cubic-to-tetragonal	Gallic acid	Up to 98	69
13	Facile co-precipitation	Spherical and cubic	CLX	40	This work

99% when using less catalyst (5 mg L^{-1} and 10 mg L^{-1}). Moreover, Table 1 compares the available literature with this work in terms of degradation efficiency, catalyst dosage, structure, and synthesis parameters. The developed material was used for the first time to evaluate the degradation of CLX. A lower amount of catalyst is required, which makes this material effective and low cost.

Photocatalytic degradation mechanism. The proposed photocatalytic degradation mechanism by $CuFe_2O_4$ NPs under UV light is presented in Fig. 11. The UV light irradiation directly excites electrons (e^-) from the valence band (VB) to the conduction band (CB) to generate an electron–hole (e^-/h^+) pair. The photo energy generated e^-/h^+ may directly degrade CLX or trigger a reactive species to degrade CLX. The e^- reacted with oxygen to generate reactive $O_2^{\bullet-}$ radicals and the photo energy-generated h^+ reacts with H_2O to produce $^{\bullet}OH$, which results in the degradation of CLX.[70]

TOC analysis. The concentrations of total organic carbon (TOC), inorganic carbon (IC), and total carbon (TC), before and after treatment of cloxacillin sodium (5 ppm) with copper ferrite NPs are presented in Fig. 12. The obtained data indicated that the TOC concentration decreased from 4.27 ppm to 2.62 ppm, which confirmed the degradation of the investigated drug. The reduced TOC value also suggested the conversion of TOC into IC, which further converted into CO_2 and H_2O. The increased concentration of IC from 0.62 ppm to 1.45 ppm after
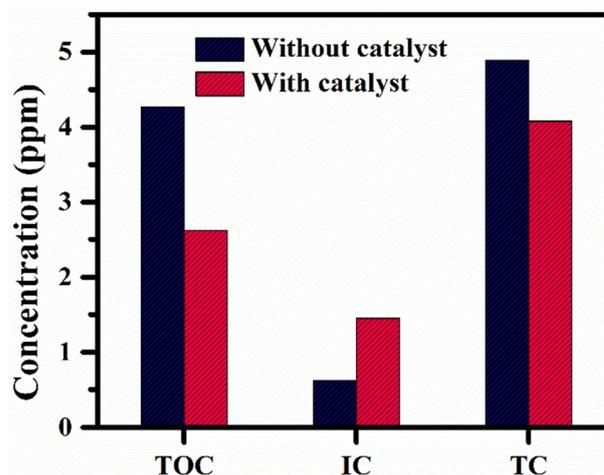

Fig. 12 Concentration (ppm) of TOC, IC, and TC in cloxacillin with and without copper ferrite NPs.

degradation also supports the conversion of TOC into IC. The value of TC was reduced from 4.89 ppm to 4.08 ppm, which may be due to the release of CO_2 to the atmosphere from the reaction system. In conclusion, 38.64% degradation was observed by TOC analysis, which is in close agreement with the other obtained analysis results.

The degradation of CLX using different catalysts is presented in Table 2. The complete degradation of CLX required a photo-Fenton process at various pH values or more time is required under UV irradiation. The $CuFe_2O_4$ NPs as photocatalysts require less time for the degradation of CLX.

Reusability

The photocatalytic stability and reusability of the copper ferrite were investigated by performing the previously indicated photocatalytic activity measurements by treating the aqueous solution of CLX (5 ppm) with the catalyst five times. The used photocatalyst was extracted from the treated CLX solution after each cycle, cleaned with deionized water, dried in an oven for an hour at 80 degrees Celsius, and then put back to use in the next photodegradation cycle. Furthermore, photocatalytic
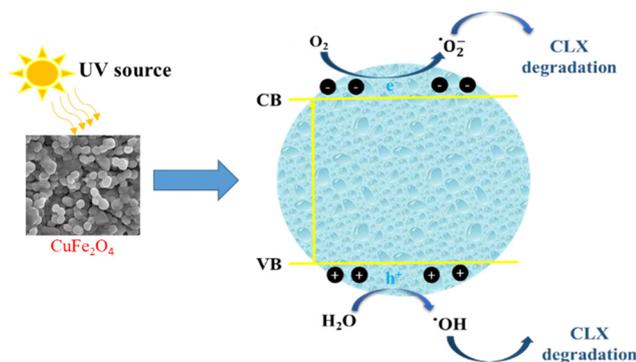

Fig. 11 CLX degradation pathway.

Table 2 Degradation of CLX using different catalysts

S. no.	Catalyst	Degradation time	pH	Efficiency (%)	Ref.
1	UV/ZnO	300 min	11	100	60
2	UV/TiO$_2$	300 min	5	—^{a}	71
	UV/H$_2$O$_2$/TiO$_2$	30 min		100	
3	UV/TiO$_2$	480 min	—	45	72
	UV/H$_2$O$_2$/TiO$_2$	240 min		15	
4	UV/TiO$_2$/H$_2$O$_2$	24 h	5	100	73
5	UV/ZnS	120 min	4.5	82–100	74
6	H$_2$O$_2$/Fe^{2+}	2 min	3	100	75
6	CuFe$_2$O$_4$	5 min	8	40	This work

^{a} Not mentioned.

stability is significant in large-scale procedures. Hence, to investigate the stability of the photocatalyst, the recycling of copper ferrite for the photocatalytic degradation of CLX under UV irradiation was carried out. The efficiency of the degradation of CLX reduced from 40% to 36% after five cycles (Fig. 13), which shows that it is stable for multiple cycles. These results show the effective and stable nature of the developed catalyst.

Experimental

Materials

All the reagents and chemicals used were of analytical grade and used without further purification. Copper chloride (99%), iron nitrate (98%), and ammonium hydroxide (30–33%) were purchased from Sigma Aldrich. Sodium hydroxide (97%) and hydrochloric acid (37%) were of analytical grade and were purchased from Sigma Aldrich.

Synthesis of copper ferrite nanoparticles

2 M copper chloride solution and 2 M iron nitrate solutions are mixed followed by the addition of 1 M solution of ammonia NH$_3$ as a precipitating agent. After adding ammonia drop by drop, precipitates are formed in the solution. The formed precipitates were separated using filter paper. The precipitates

Fig. 13 Reusability and stability of copper ferrite NPs towards cloxacillin sodium.

were washed several times with distilled water and dried in an oven at 100 °C to get a final precursor powder. The final powder was calcined in a furnace at 600 °C for 4 h to get the final copper ferrite.

Characterization of copper ferrite

The FTIR (Fourier transformed infrared) spectra were obtained using a Thermos-Scientific infrared spectrophotometer with ZnSe ATR in the range from 4000 cm^{-1} to 400 cm^{-1}. UV-visible (UV-vis) spectroscopy (UV-8000) was utilized in the range from 200 nm to 800 nm for photocatalytic activities. XRD analysis of the synthesized catalyst was performed using a Bruker D2 Phaser, and diffractometer with Cu Kα radiation. SEM with EDS analysis was performed for the elemental composition surface morphology of the photocatalyst, which was observed using scanning electron microscopy (SEM, FEI NOVA nano SEM 450). PL spectroscopy of the copper ferrite catalyst was studied using a spectrofluorometric FS5 (Edinburgh Instruments, United Kingdom) system. BET of the CuFe$_2$O$_4$ NPs was studied using a Quantachrome Nova 2200e system, Kingsville, TX. TOC analysis was performed using a Sievers 860 laboratory TOC analyzer.

Photocatalytic degradation of cloxacillin sodium

The mechanism of the photocatalytic process under UV irradiation is based on the excitation of electrons of the catalyst by absorbing energy equal to or greater than its band gap. In this case, electrons from the valence band progress to the conduction band energy level to form electron–hole pairs.[76,77] The photocatalytic activity of CuFe$_2$O$_4$ nanoparticles for the degradation of CLX was determined by using a UV lamp of a longer wavelength with an emission intensity of 365 nm and a power of 10 watts. The experiment was performed in a volumetric flask inside a wooden box. The visible lamp was 20 cm above the solution. In each experiment, 100 mL of aqueous solution of CLX with a specified concentration was dispersed into the photoreactor. Subsequently, a certain amount of photocatalyst CuFe$_2$O$_4$ was introduced into the flask, providing continuous stirring. The experiments were performed under different conditions depending on the pH value, the concentration of the drug, the dosage of the catalyst, and the time of exposure to find the best photocatalytic activity of the CuFe$_2$O$_4$ NPs. After a specified interval of time, 5 mL of the sample was collected, and finally, the sample was analyzed using a UV-visible spectrophotometer by scanning the samples from 200 nm to 800 nm. The maximum absorption for the CLX was found at 217 nm.

Effect of time

The time-dependent photocatalytic efficiency of the copper ferrite NPs was tested against a 50 ppm aqueous solution of CLX under UV irradiation. For this purpose, 20 mg of catalyst was added to 100 mL solution in a reaction vessel with continuous stirring under UV light irradiation. After time intervals of 5, 10, 15, 30, 60, 120, 180, 240, and 300 min, aliquots (5 mL) were collected and analyzed using a UV-visible spectrophotometer. The drug solution was stirred for
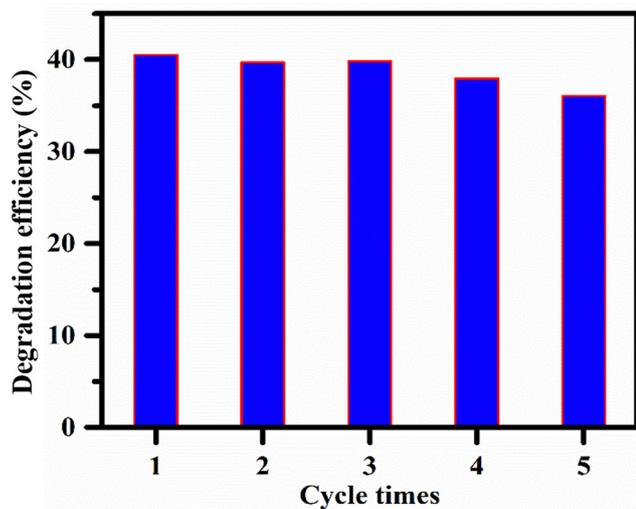
30 min in the dark before it was exposed to light. The rate of degradation of CLX solution was assessed by eqn 2.

$$\text{Degradation rate (\%)} = C_o - C_t / C_o \qquad (2)$$

Here, C_o is the initial solution's absorption intensity, and C_t is the CLX's absorption intensity after time t.

Effect of cloxacillin sodium concentration

The concentration of a drug is a key parameter in optimizing the photocatalytic degradation process. A study was performed with CLX concentrations of 5, 10, 15, 20, and 25 ppm with five different dosages of copper ferrite catalyst for the photocatalytic degradation process with a constant time of 60 min at room temperature.

Effect of solution pH

The maximum adsorption was analyzed at different pH values (4–9) of drug solution by adding 20 mg copper ferrite NPs as a photocatalyst, 5 ppm constant concentration of CLX, and 120 min for irradiation at room temperature. A phosphate buffer of pH 8 was used for sample preparation, and different pH values were adjusted using NaOH and HCl.

Effect of catalyst dose

The dosage-dependent study was carried out at 0.05, 0.1, 0.15, and 0.2 mg mL^{-1} of drug solution with different concentrations of 5, 10, 15, 20, and 25 ppm with continuous stirring under UV light for 60 min at room temperature.

Conclusions

Copper ferrite was successfully synthesized using a co-precipitation method under mild conditions. Various analytical techniques confirmed the synthesized material, including UV-visible, FT-IT, XRD, and FESEM with EDX and BET analysis. The copper ferrite has a particle size of 45 nm and a spherical shape. The average surface area for the CuFe$_2$O$_4$ NPs is found to be 65.24 m^2 g^{-1}. The calculated pH$_{PZC}$ for the catalyst is 6.64. CLX was degraded at different pH values, concentrations, times, and catalyst dosages. The TOC analysis also confirmed that the same degradation percentage as maximum degradation of CLX was observed using CuFe$_2$O$_4$ NPs as the photocatalyst under UV light irradiation. After 5 min, maximum degradation of CLX was observed, while pH-based studies confirmed the maximum degradation at pH 8 and 0.05 and 0.1 mg mL^{-1} doses are more effective for the degradation of the drug CLX. This study provides insight into the use of metal ferrites for the reduction of emerging pollutants.

Author contributions

Writing – original draft: M. N., F. H., methodology: S. A., formal analysis, A. A., S. A., and M. A. R., supervision: A. A., Conceptualization: W. A. S., writing – review and editing: M. I., K. M. B., visualization: S. H., software: M. P., validation: S. H.

Conflicts of interest

All the authors declare no conflicts of interest.

Acknowledgements

Notes and references

1 M. Mariana, H. P. S. Abdul Khalil, E. B. Yahya, N. G. Olaiya, T. Alfatah, A. B. Suriani and A. Mohamed, *J. Water Process Eng.*, 2022, **45**, 102481.

2 G. Gupta, S. K. Kansal, A. Umar and S. Akbar, *Chemosphere*, 2023, **314**, 137611.

3 A. Mostafa, *J. Biodivers. Environ. Sci.*, 2015, **7**, 501–525.

4 U. Riaz, L. Shahzad, A. Aslam, M. A. Qazi, M. Nasim, W. Anum, R. Ullah, M. M. Khan and I. Ahmad, *Abasyn J. Life Sci.*, 2022, **5**, 56–71.

5 U. Shareef, M. H. D. Othman, A. F. Ismail and A. Jilani, *J. Aust. Ceram. Soc.*, 2020, **56**, 29–39.

6 Y. Wang, X. Cui, P. Zhang, Y. Wang and W. Lu, *Environ. Technol. Innovation*, 2022, **29**, 102972.

7 E. S. Okeke, T. P. C. Ezeorba, C. O. Okoye, Y. Chen, G. Mao, W. Feng and X. Wu, *Sustainable Chem. Pharm.*, 2022, **30**, 100865.

8 C. Bouki, D. Venieri and E. Diamadopoulos, *Ecotoxicol. Environ. Saf.*, 2013, **91**, 1–9.

9 I. Michael, L. Rizzo, C. S. McArdell, C. M. Manaia, C. Merlin, T. Schwartz, C. Dagot and D. Fatta-Kassinos, *Water Res.*, 2013, **47**, 957–995.

10 Y. Ito, Y. Ikai, H. Oka, H. Matsumoto, Y. Miyazaki, K. Takeba and H. Nagase, *J. Chromatogr. A*, 2001, **911**, 217–223.

11 A. Zularisam, A. Ismail and R. Salim, *Desalination*, 2006, **194**, 211–231.

12 M. A. Zazouli and L. R. Kalankesh, *J. Environ. Health Sci. Eng.*, 2017, **15**, 1–10.

13 A. Azimi, A. Azari, M. Rezakazemi and M. Ansarpour, *ChemBioEng Rev.*, 2017, **4**, 37–59.

14 E. Mousset and K. Doudrick, *Curr. Opin. Electrochem.*, 2020, **22**, 221–227.

15 M. T. Yagub, T. K. Sen and S. Afroze, *Science*, 2014, **209**, 172–184.

16 A. Majumder, B. Gupta and A. Gupta, *Environ. Res.*, 2019, **176**, 108542.

17 A. G. Akerdi and S. H. J. Bahrami, *J. Environ. Chem. Eng.*, 2019, **7**, 103283.

18 Ö. Arar, Ü. Yüksel, N. Kabay and M. Yüksel, *Desalination*, 2014, **342**, 16–22.

19 Y. Liu, Z. Hu and J. C. Yu, *Chemosphere*, 2021, **278**, 130376.

20 P. Chen, P. Zhang, Y. Cui, X. Fu and Y. Wang, *Mater. Today Sustainability*, 2023, **21**, 100276.

21 A. Hassani, S. Krishnan, J. Scaria, P. Eghbali and P. Nidheesh, *Curr. Opin. Solid State Mater. Sci.*, 2021, **25**, 100941.

22 A. Hassani, P. Eghbali, F. Mahdipour, S. Wacławek, K.-Y. A. Lin and F. Ghanbari, *Chem. Eng. J.*, 2023, **453**, 139556.

23 E. S. Elmolla and M. Chaudhuri, *Desalination*, 2010, **256**, 43–47.

24 N. Baig, I. Kammakakam and W. Falath, *Mater. Adv.*, 2021, **2**, 1821–1871.

25 Y. Zhang, D. Pan, Y. Tao, H. Shang, D. Zhang, G. Li and H. Li, *Adv. Funct. Mater.*, 2022, **32**, 2109600.

26 A. Sudhaik, P. Raizada, S. Rangabhashiyam, A. Singh, V. H. Nguyen, Q. Van Le, A. A. P. Khan, C. Hu, C. W. Huang and T. Ahamad, *Surf. Interfaces*, 2022, **33**, 102182.

27 P. Anushkkaran, M. A. Mahadik, W.-S. Chae, H. H. Lee, S. H. Choi and J. S. Jang, *Chem. Eng. J.*, 2023, **472**, 144998.

28 J. Zhu, Y. Zhu, Z. Chen, S. Wu, X. Fang and Y. Yao, *Int. J. Environ. Res. Public Health*, 2022, **19**, 10710.

29 A. Miri, M. Sarani, A. Najafidoust, M. Mehrabani, F. A. Zadeh and R. S. Varma, *Mater. Res. Bull.*, 2022, **149**, 111706.

30 M. Kaur and K. Jeet, *J. Photochem. Photobiol., A*, 2022, **425**, 113717.

31 M. Abdo, R. Al-Wafi and M. Al Hammad, *Ceram. Int.*, 2023, **49**, 29245–29258.

32 A. Manohar, V. Vijayakanth, S. P. Vattikuti and K. H. Kim, *Phys. Mater. Chem.*, 2022, **286**, 126117.

33 A. Hassani, P. Eghbali and Ö. Metin, *Environ. Sci. Pollut. Res.*, 2018, **25**, 32140–32155.

34 P. A. Udhaya, A. Ahmad, M. Meena, M. A. J. Queen, M. Aravind, P. Velusamy, T. M. Almutairi, A. A. Mohammed and S. Ali, *J. Mol. Struct.*, 2023, **1277**, 134807.

35 A. Q. Malik, H. Singh, A. Kumar, R. Aepuru, D. Kumar, Q. Ul Ain, A. A. Bhat and A. Mubayi, *Energy Environ. Monitoring Assess.*, 2022, **19**, 744.

36 S. M. Rathod, A. R. Chavan, S. S. Jadhav, K. M. Batoo, M. Hadi and E. H. Raslan, *Chem. Phys. Lett.*, 2021, **765**, 138308.

37 S. Anandan, T. Selvamani, G. G. Prasad, A. Asiri and J. Wu, *J. Magn. Magn. Mater.*, 2017, **432**, 437–443.

38 S. Anandan, T. Selvamani, G. G. Prasad, A. M. Asiri and J. J. Wu, *J. Magn. Magn. Mater.*, 2017, **432**, 437–443.

39 A. Anantharaman, B. A. Josephine, V. M. Teresita, T. Ajeesha and M. George, *J. Nanosci. Nanotechnol.*, 2019, **19**, 5116–5129.

40 M. Ismael, *Mater. Res. Bull.*, 2022, **151**, 111803.

41 M. Israr, J. Iqbal, A. Arshad, A. Sadaf, M. Rani, M. Rani and S. Jabeen, *J. Phys. D: Appl. Phys.*, 2021, **54**, 395501.

42 M. Kılıç, N. D. Kahya, B. S. Mısırlıoğlu, Ö. Çakır and Z. G. Özdemir, *Ferroelectrics*, 2021, **571**, 183–199.

43 E. Agouriane, B. Rabi, A. Essoumhi, A. Razouk, M. Sahlaoui, B. Costa and M. Sajieddine, *J. Mater. Environ. Sci.*, 2016, **7**, 4116–4120.

44 P. Sarkar, D. Roy, B. Bera, S. De and S. Neogi, *Chem. Eng. J.*, 2022, **430**, 132834.

45 A. Mohseni-Bandpei, S. M. Ghasemi, A. Eslami, M. Rafiee, M. Sadani and F. P. Ghanbari, *J. Photochem. Photobiol., A*, 2021, **418**, 113425.

46 A. Subha, M. Shalini, B. Sahu, S. Rout and S. C. Sahoo, *Mater. Chem. Phys.*, 2022, **286**, 126212.

47 J. Singh, T. Dutta, K.-H. Kim, M. Rawat, P. Samddar and P. Kumar, *J. Nanobiotechnol.*, 2018, **16**, 1–24.

48 A. El Khanchaoui, M. Sajieddine, M. Ounacer, A. Fnidiki, F. Richomme, J. Juraszek, M. Mansori, M. Dib and A. Essoumhi, *Appl. Phys. A: Mater. Sci. Process.*, 2022, **128**, 406.

49 T. Kaur, B. Kaur, B. H. Bhat, S. Kumar and A. Srivastava, *Phys. B: Condens. Matter*, 2015, **456**, 206–212.

50 M. Ghaani and J. Saffari, *J. Nanostructures*, 2016, **6**, 172–178.

51 X. Guo, K. Wang and Y. Xu, *Mater. Sci. Eng. B*, 2019, **245**, 75–84.

52 H. Yan, Y. Zhang, Y. Wang, J. Liu, X. Li, Y. Zhang and P. Dong, *Ceram. Int.*, 2019, **45**, 20796–20802.

53 L. Plyasova, T. Y. Kardash, D. Svintsitskiy, E. Paukshtis, N. Shtertser and T. Minyukova, *Mater. Res. Bull.*, 2019, **118**, 110481.

54 K. Atacan, B. Topaloğlu and M. Özacar, *Appl. Catal., A*, 2018, **564**, 33–42.

55 P. Paramasivan and P. Venkatesh, *Phys. E*, 2016, **84**, 258–262.

56 Z. A. ALOthman, *Materials*, 2012, **5**, 2874–2902.

57 N. Masunga, B. B. Mamba, Y. W. Getahun, A. A. El-Gendy and K. K. Kefeni, *Mater. Sci. Eng. B*, 2021, **272**, 115368.

58 H. A. Kiwaan, T. M. Atwee, E. A. Azab and A. A. El-Bindary, *J. Chin. Chem. Soc.*, 2019, **66**, 89–98.

59 A. Akyol, H. Yatmaz and M. Bayramoglu, *Appl. Catal., B*, 2004, **54**, 19–24.

60 E. S. Elmolla and M. Chaudhuri, *J. Hazard. Mater.*, 2010, **173**, 445–449.

61 M. Rashad, R. Mohamed, M. Ibrahim, L. Ismail and E. Abdel-Aal, *Adv. Powder Technol.*, 2012, **23**, 315–323.

62 F. Sinfrônio, J. Rodrigues, F. Silva, R. Fonseca, A. De Menezes, R. Mouta, S. Sharma and M. Castro Jr, *J. Electron. Mater.*, 2018, **47**, 6821–6832.

63 Z. Ye, Z. Deng, L. Zhang, J. Chen, G. Wang and Z. Wu, *Mater. Res. Express*, 2020, **7**, 035007.

64 R. Priya, S. Stanly, R. Anuradha and S. Sagadevan, *Mater. Res. Express*, 2019, **6**, 095014.

65 N. Jaafarzadeh, F. Ghanbari and M. Ahmadi, *Chem. Eng. J.*, 2017, **320**, 436–447.

66 M. Rashad, R. Mohamed, M. Ibrahim, L. Ismail and E. Abdel-Aal, *Adv. Powder Technol.*, 2012, **23**, 315–323.

67 S. Naghash-Hamed, N. Arsalani and S. B. Mousavi, *ChemistryOpen*, 2022, **11**, e202200156.

68 A. Mohseni-Bandpei, S. M. Ghasemi, A. Eslami, M. Rafiee, M. Sadani and F. Ghanbari, *J. Photochem. Photobiol., A*, 2021, **418**, 113425.

69 M. V. López-Ramón, M. A. Álvarez, C. Moreno-Castilla, M. A. Fontecha-Cámara, Á. Yebra-Rodríguez and E. Bailón-García, *J. Colloid Interface Sci.*, 2018, **511**, 193–202.

70 P. Y. Motlagh, A. Khataee, A. Hassani and Y. Orooji, *J. Ind. Eng. Chem.*, 2023, **126**, 465–479.

71 E. S. Elmolla and M. Chaudhuri, *Desalination*, 2010, **252**, 46–52.

72 E. A. Serna-Galvis, A. L. Giraldo-Aguirre, J. Silva-Agredo, O. A. Flórez-Acosta and R. A. Torres-Palma, *Environ. Sci. Pollut. Res.*, 2017, **24**, 6339–6352.

73 E. S. Elmolla and M. Chaudhuri, *Desalination*, 2010, **252**, 46–52.

74 H. R. Pouretedal and M. A. Hasanali, *Desalin. Water Treat.*, 2013, **51**, 2617–2623.

75 E. S. Elmolla and M. Chaudhuri, *J. Hazard. Mater.*, 2009, **172**, 1476–1481.

76 U. I. Gaya and A. Abdullah, *J. Photochem. Photobiol., C*, 2008, **9**, 1–12.

77 M. Mariana, H. P. S. Abdul Khalil, E. B. Yahya, N. Olaiya, T. Alfatah, A. Suriani and A. Mohamed, *J. Water Process Eng.*, 2022, **45**, 102481.